Astrophysical jets: insight into long term hydrodynamics. Article and Supplementary Information.

Astrophysical jets: insights into long-term hydrodynamics

2011 New J. Phys. 13 043011

(http://iopscience.iop.org/1367-2630/13/4/043011)

New Journal of Physics
The open-access journal for physics

Astrophysical jets: insights into long-term hydrodynamics

D Tordella[1,5], M Belan[2], S Massaglia[3], S De Ponte[2], A Mignone[3], E Bodenschatz[4] and A Ferrari[3]

[1] Dipartimento di Ingegneria Aeronautica e Spaziale, Politecnico di Torino, I, Italy
[2] Dipartimento di Ingegneria Aerospaziale, Politecnico di Milano, I, Italy
[3] Dipartimento di Fisica Generale, Università di Torino, I, Italy
[4] Max Planck Institute for Dynamics and Self-Organization, Goettingen, D, Georg August University, Goettingen, D, Cornell University, Ithaca, IL, USA
E-mail: daniela.tordella@polito.it

New Journal of Physics **13** (2011) 043011 (26pp)
Received 20 November 2010
Published 12 April 2011
Online at http://www.njp.org/
doi:10.1088/1367-2630/13/4/043011

Abstract. Astrophysical jets are ubiquitous throughout the universe. They can be observed to emerge from protostellar objects, stellar x-ray binaries and supermassive black holes located at the center of active galaxies, and they are believed to originate from a central object that is surrounded by a magnetized accretion disc. With the motivations to understand whether hypersonic Newtonian jets produce any similarity to the morphologies observed in jets from young stellar objects (YSOs) and whether numerical codes, based on Godunov-type schemes, capture the basic physics of shocked flows, we have conceived a laboratory experiment and performed three-dimensional (3D) numerical simulations that reproduce the mid-to-long-term evolution of hypersonic jets. Here we show that these jets propagate, maintaining their collimation over long distances, in units of the jet initial radius. The jets studied are quasi-isentropic, are both lighter and heavier than the ambient and meet the two main scaling parameter requirements for proto-stellar jets: the ejection Mach number and the ambient/jet density ratio.

S Online supplementary data available from stacks.iop.org/NJP/13/043011/mmedia

[5] Author to whom any correspondence should be addressed.

Contents

1. Introduction

Young stars, compact objects and galactic supermassive black holes often generate astrophysical jets. These are narrow, complex projection flows along which mass, momentum, energy and magnetic flux are transported through the ambient, in either the interstellar or the intergalactic medium. They display different luminosities, from the most powerful examples that have been observed to emerge from active galactic nuclei (AGNs) down to the jets associated with low-mass young stellar objects within our own galaxy (Birkinshaw *et al* 1997, Ferrari 1998, Reipurth and Bally 2001, Gouveia dal Pino 2005; see figure 1).

In astrophysics, there is consensus about a common set of morphological properties, which are shared by most of these outflows, despite their different physical scales and power. Observations have shown that astrophysical jets are collimated, show a sequence of bright high-density regions (a chain of more or less regularly spaced emission knots) and may end in intense radiation emission areas (with line emission in the case of young stellar object (YSO) jets and synchrotron continuum emission in the hot-spots of FRII radio jets). The latter are the regions where the jets impact against the ambient medium, and are called the 'working surface' in the jet literature.

Evidence of accretion of matter onto central compact gravitating objects via an accretion disc suggests that jets may have a common origin. The mechanism proposed for jet acceleration requires the crucial contribution of magnetic fields. In the case of AGN jets, it is expected that the fraction of energy flux due to magnetic fields dominates over the kinetic energy flux in the initial regions of the jet only. Stability issues and observations imply that they become mass dominated further out (Sikora *et al* 2005, Giannios and Spruit 2006). In this paper, we will refer to YSO jets in particular, since the two main parameters, i.e. the jet ambient density ratio (which is $\geqslant$ unity) and the Mach number, will be similar in our experiment to those inferred for these objects. In contrast, there are indications that in AGN jets the density ratio is much smaller than unity. These, in addition, are moving at relativistic speeds in many cases.

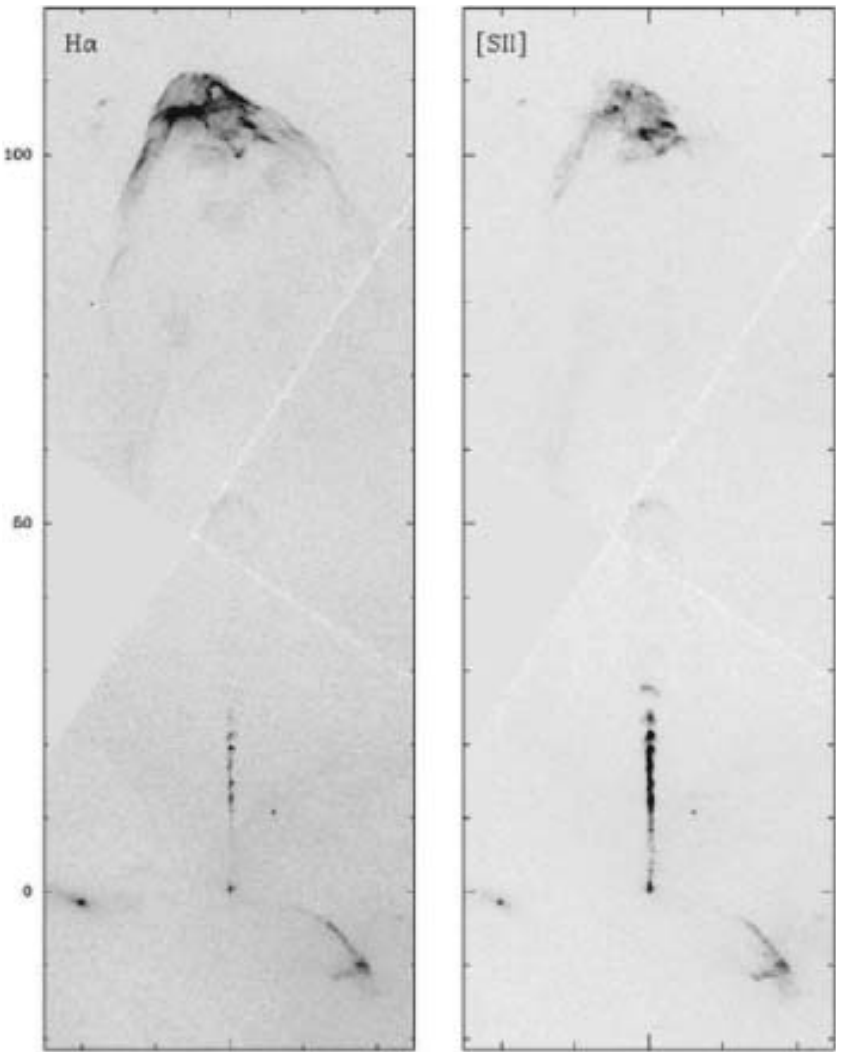

Figure 1. An example of astrophysical jets, the YSO jet HH 34. Reproduced from Reipurth *et al* (2002) by permission of the AAS.

The main challenge in designing Earth laboratory experiments to test this scenario is to achieve sufficient dynamical similarity between experiment and nature in order to capture as much physics as possible. In recent years, several controlled experiments have produced useful results and increased the trust of the astrophysical community in laboratory-based astrophysics (Bellan *et al* 2009, Cocker 2010). For example, a first set of laboratory magneto-hydrodynamical experiments for addressing time-dependent, episodic phenomena relevant to the poorly understood jet acceleration and collimation region have been carried out by Ciardi *et al* (2009). The experimental results show the periodic ejections of magnetic bubbles, generated by a pulsed-power facility. The magnetic bubbles have been studied in connection with the emitting knots observed in stellar jets. In these experiments, the jet–ambient density ratio is much larger than and the Mach number inside the jet is much lower than the typical YSO jets. However, the velocity reaches the same order of magnitude as that of the stellar jets and the structure of the magnetic field can be observed. A different kind of laboratory plasma jets have

been produced with lasers colliding on aluminum foils (Gregory *et al* 2008). The generated jets have velocities, $\sim 300\,\mathrm{km\,s^{-1}}$, that match the scaling relations for YSO jets.

Another example is the laboratory study concerning the deflection of supersonic jets produced by molecular clouds that has recently been discussed and compared with observations and numerical simulations (Hartigan *et al* 2009). The study is applied to HH110. In the laboratory, the temperature reaches a value close to the temperature observed in HH110, the speed is one order of magnitude lower, and the density is many orders of magnitude larger. The experiment provides key insights into the three-dimensional (3D) evolution of the deflected jet and yields information about where within the working surfaces multiple subsonic shells and filaments form and where along the interface shocked jet material penetrates into and destroys the obstacle along its path.

In this work, we produce prototype hypersonic jets both in the laboratory and by 3D numerical simulations. The goals are to verify that the hydrocode employed captures the basic physical processes in high-Mach-number flows through a comparison with experimental data, and to discuss how a number of aspects, which are essential features of the morphology of protostellar jets, such as the presence or absence of a cocoon and the jet persistence over distances much larger than the initial jet radius, also appear in experimental hypersonic jets where only nonlinear Newtonian hydrodynamics are applied.

To achieve these goals, we have conceived a laboratory experiment (see figure 2) where the jets are observed during a mass flow temporal growth phase in the nozzle and beyond (see figure 3). Two different ambients, lighter and heavier than the initial gas in the jet, are used in the experiment. For details of the laboratory and numerical experiment, see section 2 and the appendix.

2. Methods

2.1. The experimental setup

The laboratory experiment was carried out in an apparatus designed for the study of hypersonic jets (Belan *et al* 2004, 2008, 2010). The flows under test are jets obtained from a de Laval nozzle that propagate along the longitudinal axis of a cylindrical vacuum vessel. In this apparatus, it is possible to use different gases for the jet and the surrounding ambient in the vessel, which allow a wide variation of the nominal density ratio η as an independent parameter. The gases involved in these experiments are helium, argon, xenon and air. The vessel is modular: five different sections are available for mounting and the total length can vary from 1.4 to 4.1 m, with a constant diameter of 0.5 m. The vessel was mounted in a three-section configuration for this work. Several nozzles designed for Mach numbers ranging from 5 to 20 are available. In this study, the jets were produced using a nozzle with a nominal Mach number of 15. The gas flow in the nozzle is driven by a fast piston system, which is capable of producing the right gas stagnation conditions. The diameter of the nozzle exit section is $2r_0 = 71.36\,\mathrm{mm}$; this is also the nominal diameter of the jets. The vessel diameter is 14 times larger than the diameter of the jets. An electron gun, equipped with a deflection system, creates an electron sheet. This sheet intercepts the jet and generates a plane fluorescent section of the flow, which is then acquired by a fast CMOS camera equipped with an image intensifier (for details, see appendix A.3). The electron gun and camera can be mounted onto several ports and optical windows. Here they have been mounted in such a way as to acquire the field between nearly 24 and 28 jet diameters from

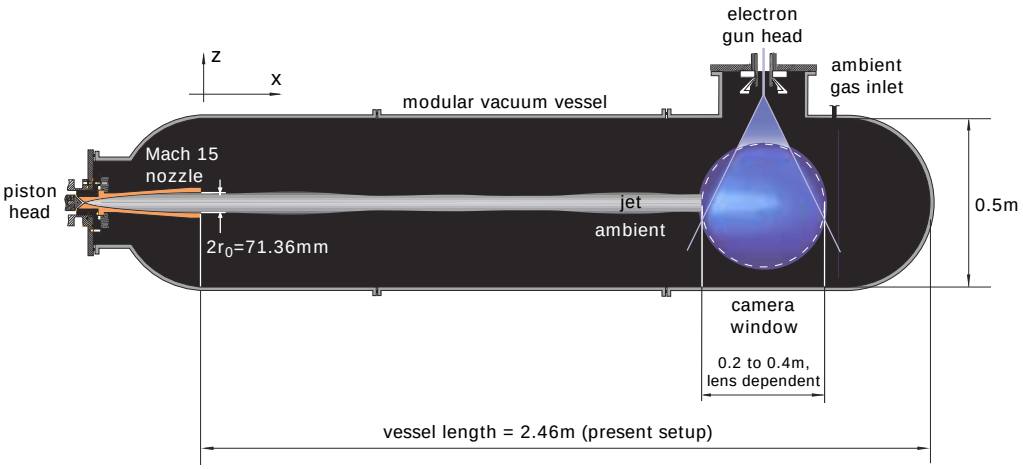

Figure 2. The experimental setup. By means of a fast piston mounted on the left, the jet gas is compressed to stagnation pressures ranging from 0.1 to 0.7 MPa, and is accelerated by a de Laval nozzle. A nozzle designed for generating a Mach 15 jet at the exit has been used in this experiment. Slightly different Mach numbers can be obtained by adjusting the stagnation/ambient pressure ratio p_0/p_a around the value 4.76×10^4. The jet travels along a vessel filled with the desired ambient gas (at pressures in the 1.5–100 Pa range) and meets an electron sheet. The sheet ionizes the gases and makes a plane section of the flow visible; these images are acquired by an intensified high-speed CMOS camera. The vessel is modular and the length is 2.46 m in the present setup. The usable optical window depends on the camera lens; it can be adjusted between 0.2 and 0.4 m in the present setup. The nozzle exit diameter is $2\,r_0 = 71.36$ mm. For further details, see the appendix.

the nozzle exit. The present configuration of the apparatus is sketched in figure 2. For details of the flow visualization technique, see the appendix, where sample films of the jets can also be found.

2.2. *Numerical simulations*

The simulations have been carried out on a 3D domain in the Cartesian coordinates (x, y, z), which are normalized over the initial jet radius r_0.

The domain has an initial jet radius size of $70 \times 14 \times 14$ initial jet radii and includes $860 \times 172 \times 172$ zones. The x-axis represents the longitudinal direction of the jet. We employed the PLUTO numerical code of Mignone *et al* (2007) for the solution of hypersonic flows. The code provides a multiphysics, multialgorithm modular environment, which is particularly oriented towards the treatment of astrophysical flows in the presence of discontinuities (Massaglia *et al* 1996, Zanni *et al* 2003). Different modules and algorithms may be independently selected to properly describe Newtonian, relativistic, MHD or relativistic MHD fluids. In this case, Newtonian hydrodynamics have been used. This module exploits a general framework for integrating a system of conservation laws, built on modern Godunov-type shock-capturing schemes.

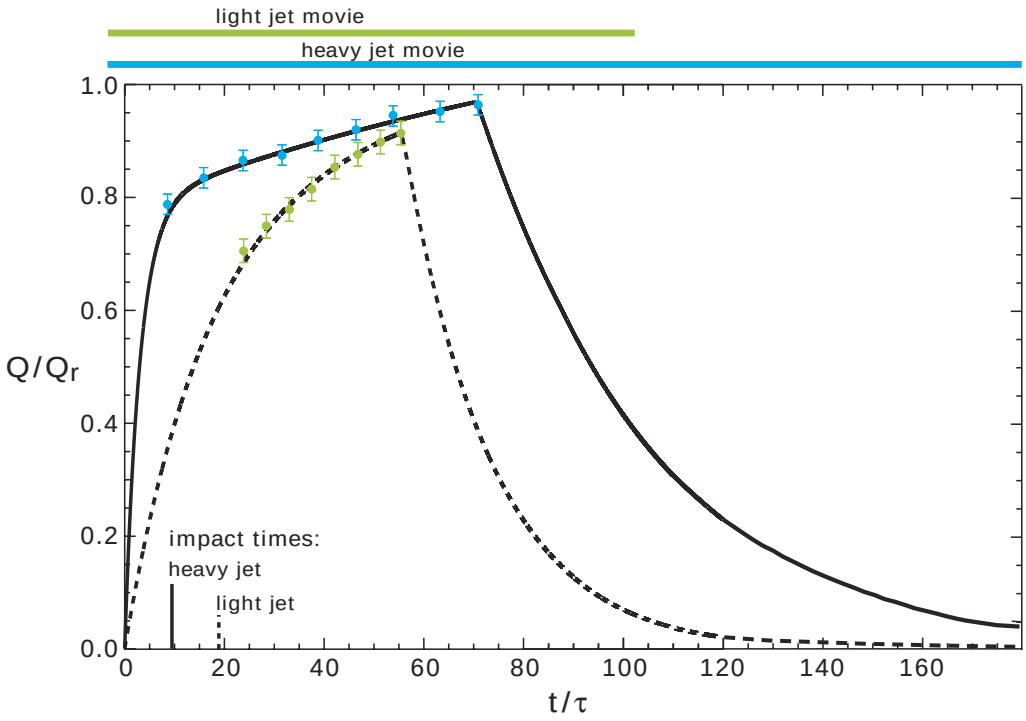

Figure 3. Jet gas injection: dimensionless nozzle mass flow versus dimensionless time. Solid line (numeric) and blue dots (experimental): heavy jet, xenon in air. Dashed line (numeric) and green dots (experimental): light jet, helium in xenon. The usable duration of the movies analyzed in this work is reported above the graphs. The mass flow Q is normalized over the reference flow rate Q_r, which is yielded by the same nozzle when operating in ideal steady conditions. For the helium jet, Q_r is $0.43\,g\,s^{-1}$, and for the xenon jet, Q_r is $2.44\,g\,s^{-1}$. Time is normalized over the jet time unit τ (the ratio between the jet radius at the nozzle exit and the speed of sound inside the jet). The piston output valves begin to open at $t = 0$. The impact times of the jets at the vessel end are indicated on the time axis. As the piston works, the outflow increases to a maximum value; then it diminishes as the gas contained in the reservoir is used up. The mass flow depends on the stagnation pressure of the nozzle flow p_0. During the increasing phase, the mass flow also depends on a modulation factor $f(t)$ associated with the opening time history of the piston valves. During the decreasing phase, the mass flow is determined by the natural decay in the amount of gas remaining in the piston chamber. The stagnation pressure p_0 can be measured in the compression phase by a pressure transducer put in place of the de Laval nozzle; for details see the appendix (in particular section A.1 and the film piston.mov).

To reproduce the actual cylindrical vessel in our Cartesian 3D domain, and after exploring different possibilities, we devised a set of internal conditions for the lateral boundaries, defined where the cylindrical radius $r = \sqrt{y^2 + z^2}$ is equal to seven jet radii and where we imposed that all the velocity components vanish and density and pressure are fixed to the initial values. For more details, see appendix D. The conditions on the right boundary of the domain are reflective.

The jet is injected at the left boundary, where the conditions must take into account the initial transient. The jet density is in units of the on-axis initial jet density in ideal conditions, i.e. with injection ideally given by a step function in time (see figure 3 for the real—experimentally determined—injection laws). To check the influence of the lateral wall on jet development and in particular on its entrainment properties, numerical simulations were also carried out by using a lateral free-boundary condition. The difference that emerged was not substantial (see appendix D.1).

The boundary condition on the left can be written, for the different variables, as

$$\rho = \rho_a + \frac{\rho_{jet} - \rho_a}{\cosh(r^n)}, \tag{1}$$

$$v_{y,z} = 0, \tag{2}$$

$$v_x = \frac{v_{jet}}{\cosh(r^n)}, \tag{3}$$

$$p = p_a + \frac{p_{jet} - p_a}{\cosh(r^n)}, \tag{4}$$

where ρ_a and p_a are the (constant) density and pressure of the ambient gas (at a vacuum chamber/laboratory temperature T_a of 298 K) and $n = 8$. Equations (1)–(4) represent the density, velocity and pressure profiles at the output of the real nozzle. The quantities ρ_{jet}, v_{jet} and p_{jet} grow with time, consistent with the behaviour of the experimental injection device, and eventually decline as the gas contained in the reservoir is used up (see figure 3). Ideally, for an infinite reservoir of gas, we would have

$$\frac{\rho_{jet}}{\rho_a} \to \eta, \quad \frac{p_{jet}}{p_a} \to 1, \quad v_{jet} \to \text{constant}. \tag{5}$$

We have modelled these transient injection conditions to mimic the actual behaviour of the experimental setup. The mass flow Q is a function of time of the kind $Q = Q[p_0(t), f(t), g(t)]$, where p_0 is the pressure in the piston chamber (neglecting the friction, p_0 is the stagnation pressure of the nozzle flow), $f(t)$ is a factor function that accounts for the way the nozzle flow is accelerated by the fast piston device and $g(t)$ is the function that accounts for the final decay phase due to the emptying of the gas from the piston chamber. This model, which is based on piston-valve behaviour, gives the following behaviour for the density, pressure and velocity of the gas at the nozzle exit during the increasing phase,

$$\rho_{jet} \sim Q(t)^{2/3}, \quad p_{jet} \sim Q(t)^{4/3}, \quad v_{jet} \sim Q(t)^{1/3}. \tag{6}$$

The derivation of these formulae is detailed in appendix D (see pp 22–25).

Using a convolution technique on the numerical images, we have also approximated the visual filtering to the laboratory images by the fast CMOS camera. This allows the loss of the visual contrast, which is typical of the camera observation images, to be simulated (see again appendix D.2).

3. The physical parameters

Observations (see reviews by (Reipurth and Bally (2001) and Gouveia dal Pino (2005)) point out that jets from YSOs have a Mach number $\mathcal{M}_{obs} = 10$–40, a jet–ambient density ratio

$\eta_{\rm obs} \approx 1$–10 and a Reynolds number exceeding 10^{10}. Although the length scales are very different in the laboratory from astrophysical systems, experiments can be designed in which the critical dimensionless parameters, such as the Mach number and the density ratio, have similar values. Those that are larger in astrophysical systems, such as the Reynolds number, are sufficiently large for the experiments to capture the asymptotic behaviour. It should be noted that, as long as radiation transport and relativistic and magnetohydrodynamic effects can be ignored in the astrophysical situation of interest, the scaling between the experimental system and the corresponding astrophysical systems will primarily depend on these two parameters, i.e. the internal Mach number, $\mathcal{M}$, of the jet and the jet–ambient density ratio η.

As far as the jet evolution is concerned, crucial parameters are the jet length-to-radius ratio and jet lifetime in units of the sound crossing time (over this radius). YSO jets have a wide range of lengths that span from about 0.1 to a few parseconds. Jet radius can be constrained by observation above an angular distance from the source typically larger than 0.1 arcseconds, where the jet radius can be resolved in about 10^{13} m; therefore the actual jet length-to-radius ratio is in the range of a hundred to a few thousand radii. Models of the jet acceleration that deal with the jet-accretion disc system (e.g. Zanni *et al* (2007), Matsakos *et al* (2008, 2009), Tzeferacos *et al* (2009) and references therein) predict that the jet has a radius at its base well below 1 AU and grows with distance from the protostar. Therefore, our observational reference is the resolved jet radius and not the one at the base. Keeping this in mind, our numerical and experimental study covers a jet length of 70 radii, compared to real astrophysical lengths that span from about a hundred to a thousands of jet radii.

An estimate of the actual sound crossing time in YSO jets is rather difficult, since we do not observe the jet medium directly, but regions of this that have undergone shock compression and heating. A fair estimate of the pre-shock jet temperature would be about 10^3 K, corresponding to a sound speed of 3×10^3 m s^{-1}. This yields a sound crossing time or jet time unit of 100 years, which has to be related to a life time of 10^4–10^5 years. Thus the typical lifetime is 10^2–10^3 time units for YSO jets. We will see in the following that we can explore, for the light jet experiment, 70 jet radii, corresponding to up to 20 time units, before the jet head hits the chamber front wall.

Our jets are generated in a quasi-isentropic way by means of a de Laval nozzle. Due to the way the piston works, which is described in the appendix, the jet injection into the chamber is not ideal or instantaneous, but follows a time-dependent pattern (see figure 3). We define the values of the parameters corresponding to a nozzle operating in ideal steady conditions as 'nominal'.

The nominal Mach number at the nozzle exit is $\mathcal{M} = 15$ and the Reynolds number (defined as $2r_0\mathcal{M}c/\nu$, where c is the speed of sound and r_0 is the jet radius at the nozzle exit) is of the order of 10^5, which is expected to be sufficiently high to represent near asymptotic conditions. Inside the de Laval nozzle, the dissipation is only due to the presence of the boundary layer along the walls. The nozzle is always operated in pressure matched, or almost matched, conditions. This prevents the formation of normal shocks inside the nozzle and at the exit. The physical time scale τ is defined as the ratio between the jet radius at the nozzle exit r_0 and the speed of sound inside the jet and in nominal conditions, and is of the order of 1 ms for the pressure-matched heavy jet and 0.2 ms for the pressure-matched light jet.

In the following, we will express time in units of τ, which depends on the jet under test, and length in units of r_0, which is a constant due to the nozzle shape. The outflow accelerated phase time interval is of the order of 100τ (50τ for the light jet and 70τ for the heavy jet, see figure 3). The stagnation pressure p_0 of the jets (at 500 K $< T_0 <$ 1000 K) can be varied in

the 0.1–0.7 MPa range. By means of a controlling set of valves, the pressure in the vessel can be adjusted from 1.5 to 100 Pa. Stagnation pressures are measured to 1% accuracy, while the pressures in the vessel are monitored by means of two 0.25% accuracy transducers, which range from 0.01 to 10 Pa and from 0.1 to 100 Pa. The ideal stagnation-to-ambient pressure ratio p_0/p_a necessary for obtaining Mach 15 is 4.76×10^4.

Our experiment has been designed to test the universal phenomenologies in Newtonian dynamics, regardless of the presence of a magnetic field. We have thus set up a first experiment in the hydrodynamic limit where these two parameters are in similitude with astrophysics. In this case, we simulate a light jet with nominal $\eta = 0.72$ (helium in xenon). This captures well the YSO jet, where we have seen that the jet density is usually close in value to, or not much higher than, the ambient one. In a second kind of experiment, we are simulating heavy jets (which are almost ballistic) in order to monitor a change in the flow patterns. Here, the jet is dense and its ambient/jet density ratio is two orders of magnitude larger ($\eta = 102$, xenon in air), but the nominal Mach number remains the same.

A set of corresponding numerical simulations has been carried out on a 3D domain in the Cartesian coordinates, using the PLUTO numerical code described above.

4. Morphological properties of the hypersonic jet Newtonian dynamics

The flow visualizations of the intermediate-far field of the jet spatial evolution of the experiments are shown in figures 4 and 5 for jets that are lighter than the ambient and in figures 7 and 8 for jets that are heavier than the ambient.

The visualizations of the light jet are compared with 2D cuts in the longitudinal plane of the density distribution at two different time instants of the simulations. The experimental images are taken during a laboratory observation interval of $10.2\,\text{ms} \simeq 56\tau$; in this lapse of time, the camera acquires 51 images. The visualization technique adopted in the experiment also allows us to reconstruct longitudinal jet sections; thus the laboratory and numerical images can be compared (see appendices B and A.3). Figure 4 shows the light jet before impact with the right wall of the chamber; one sees the bow shock, the cocoon and the reflection at the lateral boundaries. One can also see the compression shocks along the jet caused by the cocoon backflow, which generates a shear that acts on the inner part of the jet. The images in figure 5 have been taken at $1.44\,\text{ms} = 8\tau$ after the jet head hits the right wall. One intense knot is visible on the jet axis, about ten jet radii from the vessel end, in both the actual jet and the simulated one (the simulation uses reflective b.c.s; for details, see appendix B.2. This knot is due to the matter reflected at the vessel end; the differences in the simulated and experimental positions are for the most part due to measurement errors, but also to the uncertainties in the injection modelling, as explained in what follows. In the simulations, the jet head (bow shock) velocity grows from $v_{\text{sim}} = (440 \pm 3)\,\text{m s}^{-1}$ to $v_{\text{sim}} = (706 \pm 3)\,\text{m s}^{-1}$ (or 2220–3560 r_0/τ) in the $2\tau < t < 16\tau$ time interval, due to the increase in mass flow. This time interval precedes impact with the end wall. The experimental head velocity at $t = 15\tau$ is measured by means of image correlation (see appendix B, p 19–22) and is equal to $v_{\text{exp}} = (490 \pm 140)\,\text{m s}^{-1}$ or 2470 r_0/τ. The velocities v_{sim} and v_{exp} could be compared at $t = 15\tau$, where $v_{\text{sim}} = 687\,\text{m s}^{-1}$. This value is remarkably higher than the corresponding experimental value v_{exp}. This significant difference can be explained by, on the one hand, the large uncertainty on v_{exp} due to the image noise and blur, i.e. the shift of the subject along an exposure time and, on the other, by the source of error on v_{sim} linked to the way the numerical injection curve represents the real one. In fact, the numerical injection curve

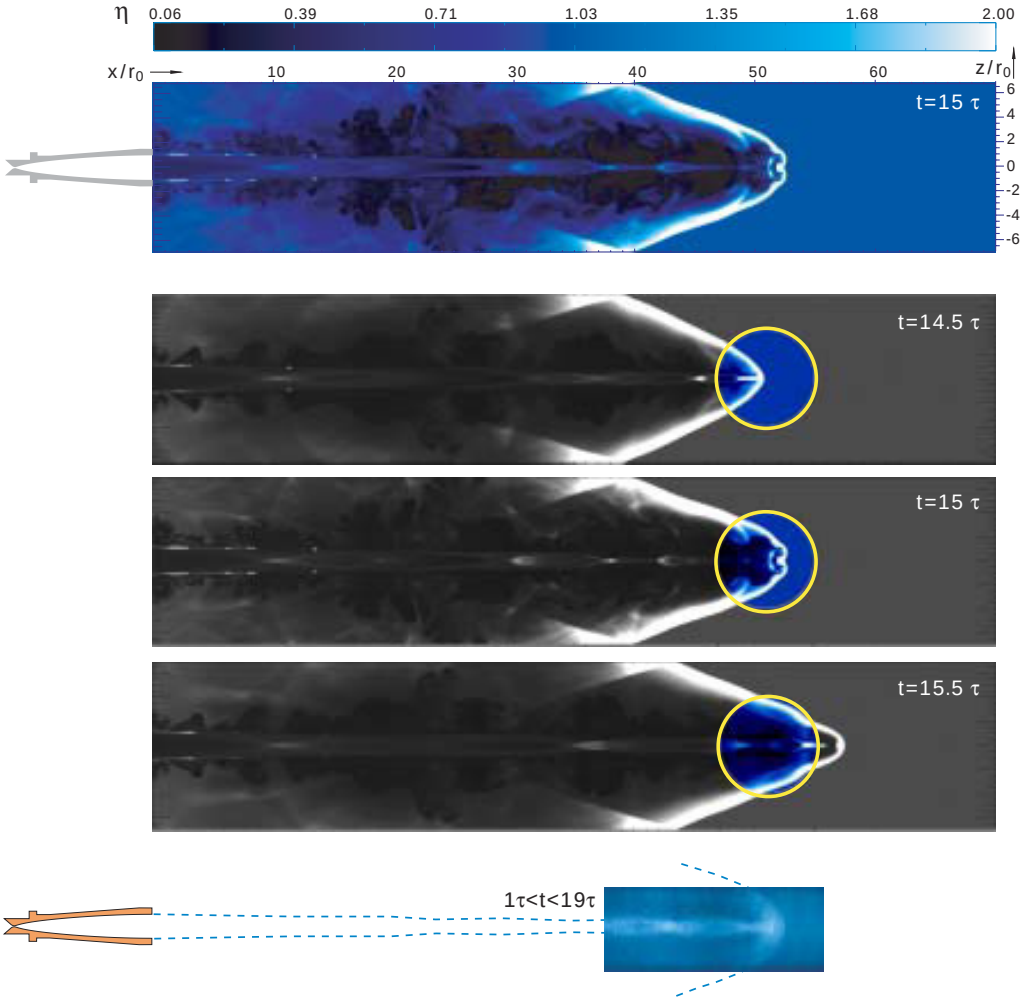

Figure 4. Light jet, helium in xenon. $\mathcal{M} = 16.1$, ambient pressure $p_a = 4.0 \pm 0.1$ Pa, estimated nozzle exit velocity $= (3200 \pm 330)\,\mathrm{m\,s^{-1}}$, mean jet pressure at the nozzle exit $p_j = p_a \pm 30\%$, stagnation/ambient pressure ratio $p_0/p_a = 7 \times 10^4 \pm 30\%$. The space unit is the exit radius of the nozzle $r_0 = 0.035\,68$ m. The time unit for this light jet is $\tau = 0.18$ ms. Top panel: numerical simulation, density map at time instant $t = 15\tau$. The density is normalized to the unperturbed ambient value. Second to fourth panels: numerical sequence of 3 time instants, an optical window having the same size of the laboratory one is highlighted on each panel. Last panel: laboratory visualization, superpositions of scaled correlated frames on a time range including the numerical simulations shown above, the details of the image reconstruction method are given in appendix B.

is either partly interpolated (the initial and intermediate phases) or partly modelled (the ultimate damping phases) on the experimental data, which are affected by the uncertainties (about 6–7%) in the measurement of the gas pressure and piston position (see the error bars in figure 3). This produces an increase in the total uncertainty σ_{sim} of v_{sim} from values less than 1% to values around 7%, i.e. $v_{sim} = (687 \pm 50)\,\mathrm{m\,s^{-1}}$. This analysis shows that the lowest numerical value $v_{sim} - \sigma_{sim} = 637\,\mathrm{m\,s^{-1}}$ can coexist with the highest experimental value $v_{exp} + \sigma_{exp} = 630\,\mathrm{m\,s^{-1}}$.

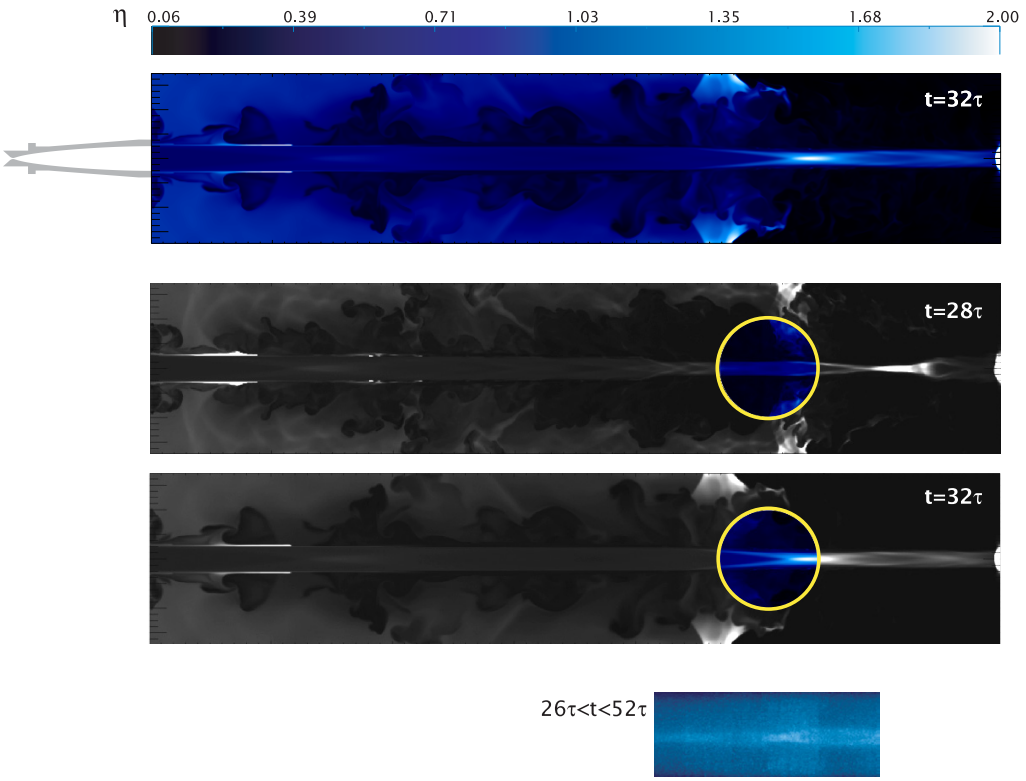

Figure 5. Light jet, helium in xenon. Same as in figure 4. Here, the images shown were taken in a time range that came after the instant where the jet head hit the vessel end.

In the simulation, before the impact, the knots behind the head move with different velocities and change in shape rapidly; the velocity range for the first three knots behind the head is $180 < v < 380\,\mathrm{m\,s^{-1}}$ (or 908–1816 r_0/τ) in the $14\tau < t < 16\tau$ time interval. The first knot behind the head that is visible in the laboratory visualization has an approximate velocity of $300 \pm 200\,\mathrm{m\,s^{-1}}$ (about 1500 r_0/τ).

It can be seen that the interaction with the reflected flow has not spoiled the axial-symmetry of the flow. It is also noticeable that the inner part of the flow remains compact and collimated after the impact. This is also interesting information, which could open the way to other applications, in particular to perturbative near-linear experimental studies. The inertial effects, and the associated compressibility, must here be exceedingly powerful to inhibit the spatial growth of the jet, unlike what occurs in the incompressible situation, where sheared flows spatially thicken (Ricou and Spalding 1961, Brown and Roshko 1974, Turner 1986, Sreenivasan and Prasad 2000, Tordella and Scarsoglio 2009).

The density distribution along the jet axis of the light jet is shown in figure 6, where we show the direct comparison between the experimental values, top panels, and the ones derived from the numerical simulations. As explained in the caption, we can clearly recognize four features in the measured values and the simulation at $t = 15\tau$, which correspond to the bow-shock and three compression knots. The compression for a xenon ideal normal shock at $\mathcal{M} = 15$ is about 3.9, a value that is well approximated in the simulations. In the laboratory observation, the position of the normal shock is clearly visible, but the density cannot be determined because

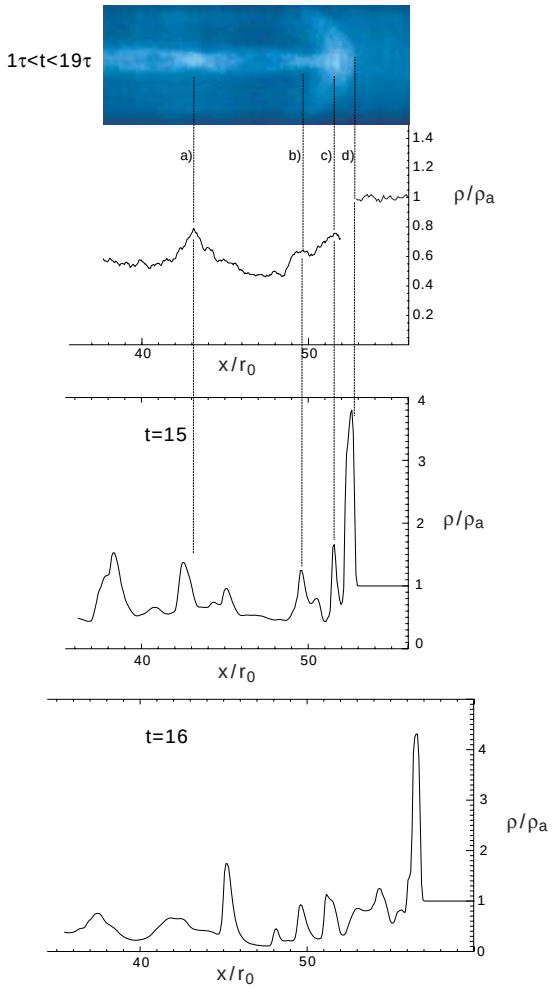

Figure 6. Light jet, helium in xenon. Top panel: laboratory visualization, the sequence of image frames for $1\tau < t < 19\tau$. The same picture as that shown in figure 4. Below, the relevant axial density distribution, normalized over the density of the unperturbed ambient gas (Xe), can be observed. In the other two panels, one can see the density distribution of the same jet numerically simulated at $t = 15\tau$ and 16τ. From left to right: line (a) density knot, line (b) density knot, line (c) terminal shock (He flows at nearly $3000\,\mathrm{m\,s^{-1}}$ and then abruptly decelerates and compresses) and, line (d) bow shock that transfers momentum to and compresses the ambient gas. Along the jet axis, between lines (c) and (d), both gases, the ambient gas and the jet gas, are present. As a consequence, the density cannot be determined in this region, because a monochromatic image does not contain enough information to distinguish the gas concentrations and thus to associate a pixel intensity with a density value. Colour images should be used (see [2,3]), but colour cameras sufficiently fast and sensitive to film the jets of the present experiment are not yet available. By comparing the numerical simulations at $t = 15\tau$ and $t = 16\tau$, it can be seen that the situation is quickly nonlinearly evolving. The two snapshot density distributions are only qualitatively similar.

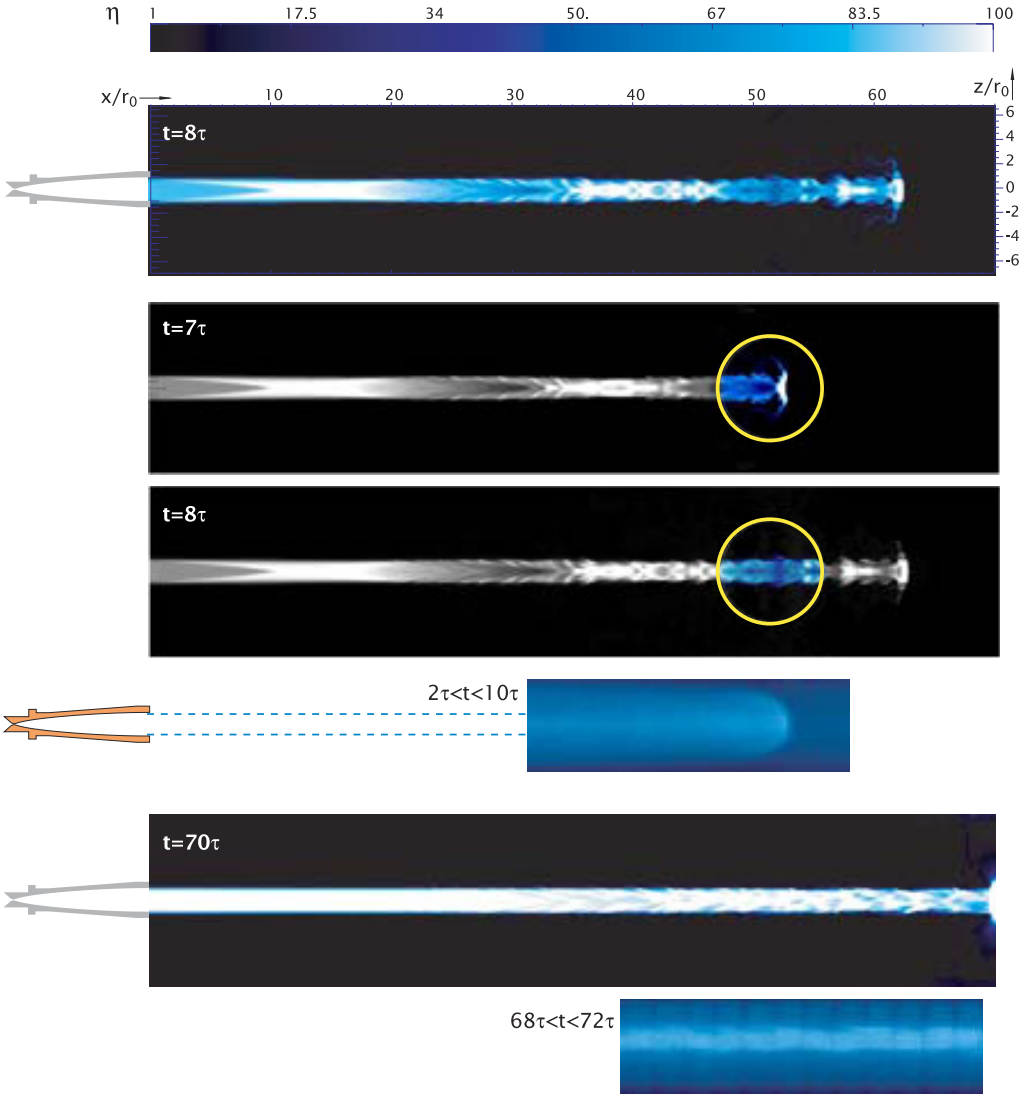

Figure 7. Heavy jet, xenon in air. $\mathcal{M} = 15$, ambient pressure $p_a = 9.95 \pm 0.1$ Pa, estimated nozzle velocity at the exit $= (560 \pm 60)\,\mathrm{m\,s^{-1}}$, mean jet pressure at the nozzle exit $p_j = p_a \pm 30\%$, stagnation/ambient pressure ratio $p_0/p_a = 4.76 \times 10^4 \pm 30\%$. The space unit is the exit radius of the nozzle $r_0 = 0.03568$ m. The time unit for this heavy jet is $\tau = 0.96$ ms. Top panel: numerical simulation, density map at time instant $t = 8\tau$. The density is normalized to the unperturbed ambient value. The second and third panels: numerical sequence of two time instants; an optical window having the same size as the laboratory one is highlighted in each panel. The fourth panel: laboratory visualization, superpositions of scaled correlated frames on a time range including the numerical simulations shown above; the details of the image reconstruction method can be found in appendix B. The fifth and sixth panels: numerical simulation and laboratory visualization, in a time range that comes after the instant where the jet head hits the vessel end.

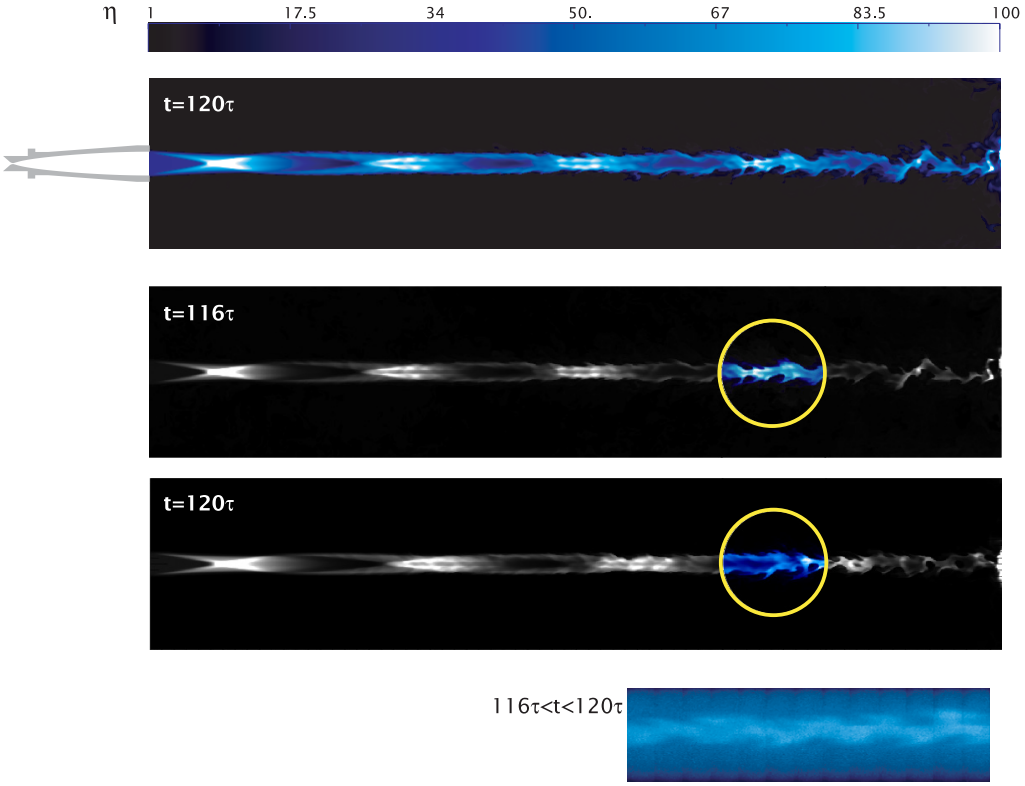

Figure 8. Heavy jet, xenon in air. The same jet of figure 7; the panels have the same meaning but the images are taken in a time range that comes well after the jet head hits the vessel end, during the mass flow decaying phase shown in figure 3.

of the presence of a mixing region near the contact discontinuity between the two gases. This region cannot be analysed by means of a monochromatic image. In fact, it is not possible to associate a pixel intensity with a density value if two different gases are present in the same zone.

The laboratory images compare very well with the numerical ones, considering the resolution of the images acquired by the fast camera (Phantom V7.1). Under the extreme conditions of the present experiment, it is necessary to balance two opposite needs, namely a short exposure to obtain sharp images and a long exposure to obtain a sufficient light level. The present images were obtained at 5000 frames s^{-1} with an exposure of 195 μs. The displacement of the jet structures, such as the bow shock, is not negligible over the exposure time. This induces a longitudinal blur, which is about 3 times more intense in the light jet than in the heavy one. We have treated the highly resolved numerical simulation with a filter that represents the virtual camera observation window. The result is very similar to the laboratory images and is described in the Supplementary data, subsection 4.2. The blur effect is also the reason for the difference in height of the density peaks in the simulation and in the experiment: for example, peak (c) in figure 6, the third panel, is so sharp that in the experimental image, under stationary conditions, it should produce a narrow impulse of very high intensity pixels. Unfortunately, its displacement distributes the light over a larger number of pixels of lower intensity and yields a lower value for the measured density peak.

Figures 7 and 8 illustrate the evolution of a heavy jet propagating through the ambient and hitting the vessel end, remaining almost unperturbed by the interaction with the external medium. The visualizations are compared with 2D longitudinal cuts of the simulated density distribution at three different time instants. The experimental images are taken during a laboratory observation interval of 115.2 ms $\simeq 120\tau$; in this lapse of time, the camera acquires 576 images. At later stages, when the jet weakens according to the behaviour in figure 3, this interaction causes non-symmetrical oscillations that are visible in both simulated and real jets. In this case, the jet head velocity grows from $(130 \pm 3)\,\mathrm{m\,s^{-1}}$ to $(270 \pm 3)\,\mathrm{m\,s^{-1}}$ (or from 3500 to 7260 r_0/τ) in the $2\tau < t < 9\tau$ time interval, and the experimental value at $t = 8\tau$ is $(140 \pm 30)\,\mathrm{m\,s^{-1}}$ or 3770 r_0/τ. The interaction with the reflected flow eventually produces a finite perturbation, which nonlinearly interacts with the outflow. This is sufficient to spoil the axial symmetry. However, it is not sufficient to spoil the collimation of the jet. This suggests the possibility of a very large longitudinal extent of the heavy hypersonic jet and its related capability to transfer energy, momentum and mass to large distances (on the Earth, in space and in possible new applications).

As mentioned before, in the light jet case, the perturbations caused by the fluid backflowing after interaction with the end wall of the vessel do not spoil the jet axial symmetry, whereas they do in the case of a heavy jet, both in the experiment and in the simulations. One must consider that the heavy jet lives longer and carries about two orders of magnitude more momentum and mass fluxes than the light one. Thus, the backflowing material interacts with the jet, forming a strong shear layer whose instabilities have time to develop asymmetric modes that eventually prevail and can be observed in figure 8.

5. Conclusions

We have carried out a joint, experimental and numerical, study of the propagation of hypersonic jets under physical conditions that mimic, in some aspects, the behaviour of protostellar jets. We have shown that the results of numerical simulations agree, within experimental errors, with the data collected in the laboratory that concern the global morphologies, the jet head advance speed, the formation and structure of knots and the jet final fate. This methodology allows us to gain some insights into the behaviour of hypersonic flows and is an important validation of the numerical tools as well.

Moreover, our experiment has highlighted the following aspects that are common to protostellar jets: (i) the near-isoentropic jets remain confined over distances much larger than the initial radius; and (ii) the presence of a cocoon surrounding the light jet, whereas this is not visible for the overdense one. These are therefore properties of high-Mach-number Newtonian jets, which capture some features of the morphology of astrophysical jets with hypersonic jet experiments produced in an Earth laboratory and in numerical simulations. These results confirm that hypersonic jets can propagate over long distances without external confining mechanisms, e.g. magnetic fields.

We have discussed in this paper two extreme cases of jet-to-ambient density ratios for a fixed Mach number. In a forthcoming paper, we plan to address also the cases of intermediate density ratios and different Mach numbers for exploring the influence of their combination on the jet evolution. Moreover, we plan to improve the jet injection system into the chamber to minimize the initial transient to bring the jet parameters as close as possible to the nominal ones.

Acknowledgments

DT thanks Robert Breidenthal, Anatol Roschko, Tullio Regge and Mario Macri' for enlightening discussions and suggestions during the conceiving and design phase of the experiment. DT and SD thank Vittorio Giavotto for making available a first basic configuration of the vacuum chamber. The de Laval nozzles were built at CERN, EST EST Division. In this regard, we sincerely thank Noel Mezin. We also acknowledge Domenic D'Ambrosio who carried out the numerical testing of the flow of the designed de Laval nozzles. The numerical calculations were performed at the CASPUR Supercomputing Facility. The project was carried out with funding from ASI and PRIN-MIUR. We warmly thank Amalia Finzi for support and encouragement. We also thank an anonymous referee for useful comments and suggestions.

Appendix A. Details of the experiment setup

A detailed view of the equipment used in this experiment is shown in figure 2. The desired vacuum level in the vessel is maintained by means of suitable multi-stage pumps, which are capable of a volume flow of $0.075\,\mathrm{m^3\,s^{-1}}$.

A.1. Details of how the piston works

The nozzles are driven by a fast piston, which operates by means of compressed air and compress the gas of the jet in the chamber that leads to the nozzle inlet (see figure A.1). This device is normally held by an electromagnet: the magnet can be turned off at any desired time. The piston run can be started and the test gas compressed in an almost isoentropic way. The piston has an annular shape. It slides between two coaxial cylinders, and it is provided with a cylindrical extension that has a set of ports, placed on a ring (see movie 1, available from stacks.iop.org/NJP/13/043011/mmedia). The inner cylinder is connected to the nozzle inlet through a second ring of ports. The two port sets form a valve system that is closed during the piston run and open when the compressed gas reaches the desired stagnation conditions. When the piston reaches this position, the two sets of ports match each other and the compressed gas flows into the nozzle. This design ensures very good repeatability of the jet at each piston run. Ideal valves do not exist; therefore the jet mass flow has an increasing and a decreasing phase, which last a measurable time, as explained in the main text.

A.2. Gases used in the experiments

The ambient in the vessel is set for each run of the experiment at the desired pressure or density just before the piston starts, thanks to a time-controlled solenoid valve mounted on the vessel side. The gases involved in these experiments are helium, argon and xenon and air. Only the first 3 gases are used for the jet, since the nozzles are designed for monoatomic gases. The jet/ambient pairs tested so far are listed in table A.1.

The Reynolds number value based on the nozzle exit diameter for the jets produced by the $\mathcal{M} = 15$ nozzle can be estimated under ideal conditions and it ranges from 1.6×10^4 for He jets at stagnation pressures and temperatures of the order of 2.5×10^5 Pa and 1000 K (nozzle exit velocity of the order of $3200\,\mathrm{m\,s^{-1}}$, $\nu_{\mathrm{He}} \simeq 0.0128\,\mathrm{m^2\,s^{-1}}$) to 4.0×10^5 for Xe jets at stagnation

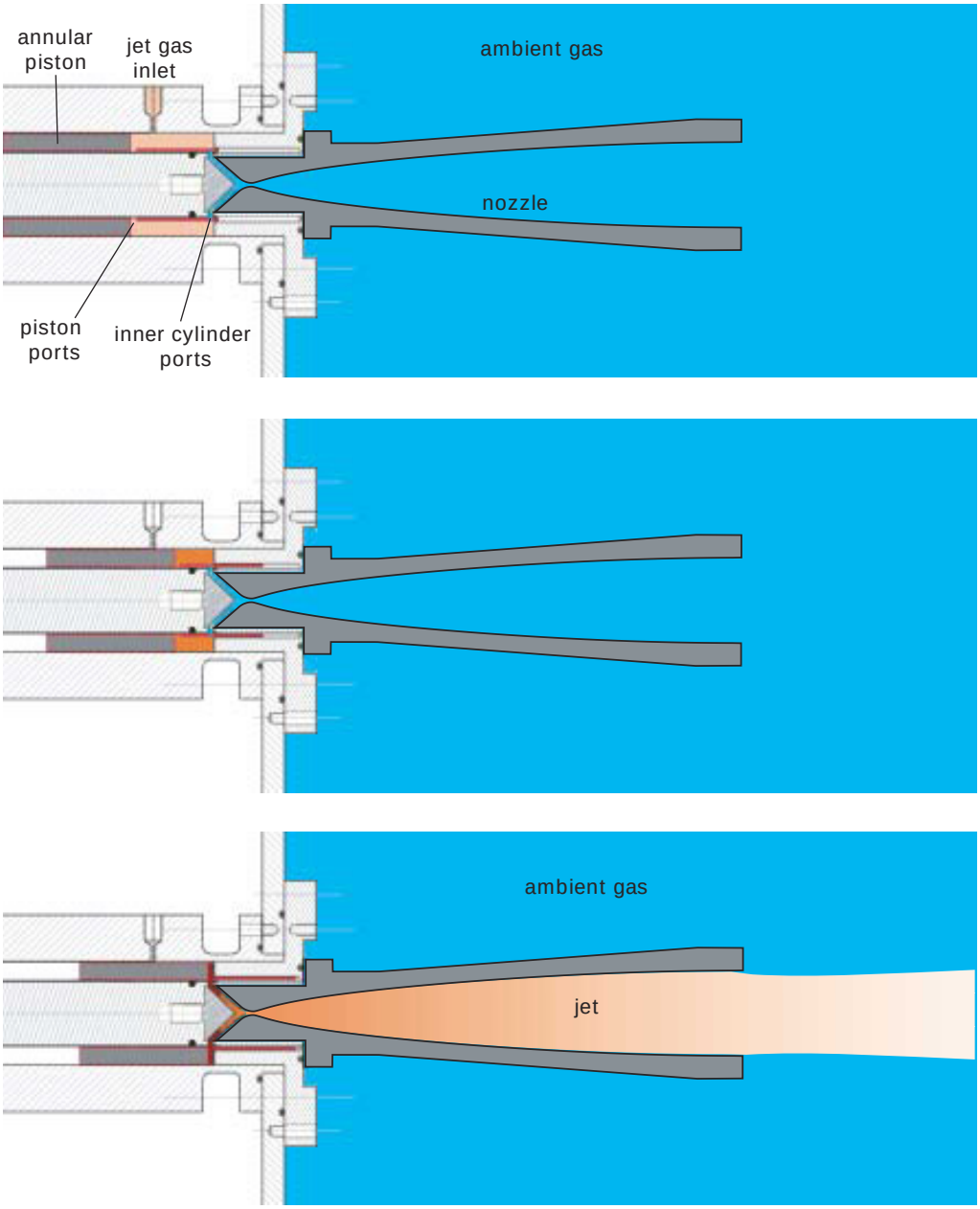

Figure A.1. Longitudinal sections of the piston–nozzle system. The piston is shown at three positions in sequence. Top panel: the initial position, after the jet gas loading. Middle panel: an intermediate time instant of the gas compression. Bottom panel: the final position, when the sets of ports match each other and the compressed gas flows into the nozzle.

pressures and temperatures of the order of 5×10^5 Pa and 500 K (nozzle exit velocity of the order of 400 m s^{-1}, $\nu_{Xe} \simeq 7.1 \times 10^{-5}$ m^2 s^{-1}). To determine these Reynolds numbers, we estimated the low-temperature values of the gas kinematic viscosity from the databases available in Hollis 1966, Kestin *et al* 1984, Grisnik 1998.

Table A.1. Experiment list. The number of tests performed for a given jet/ambient pair are shown. A film was stored in the database for each test. The various combinations of jet/ambient composition are still under analysis, and the post-processing has not yet ended for all of the combinations. At the moment, we have tested one Mach (M = 15) and the two extreme values of the jet/ambient gas density ratio we could observe. From the preliminary analysis of the combinations in this table, it seems that above the value 10 of the jet/ambient gas density ratio, the jet behaviour is very similar to what is shown in figures 7 and 8 of the main paper for xenon in an air jet.

Ambient	Jet		
	He	Ar	Xe
He		Seven tests	Eight tests
Air	Three tests	13 tests	Three tests
Ar	Two tests		10 tests
Xe	12 tests		

A.3. Visualization and measurement techniques

The visualizations and measurements are based on the electron beam method. An electron gun, operating at between 12 and 16 kV, capable of beams of up to 2 mA, was employed. The gun is equipped with a deflection system that creates an electron sheet, that intercepts the jet and generates a plane fluorescent section of the flow. This is then acquired by a fast CMOS camera (Phantom V7.2 in this experiment; other cameras equipped with an Hamamatsu V8070U image intensifier are at present being tested). This setup was used to obtain 512×512 or 768×768 monochromatic images at a frame rate of 2000–5000 fps, with an exposure time of 195 μs. The electron gun and camera can be mounted onto several ports and optical windows. In this case, they were mounted in such a way as to acquire a field between about 47 and 55 jet radii from the nozzle exit.

The gas density can be measured by means of the well-known linear relation

$$\rho = k_g I, \tag{A.1}$$

where I is the intensity (pixel value) taken from a subregion of the image and k_g is the constant of the tested gas (Brown and Miller 1957, Muntz 1968, Bütefisch and Vennemann *et al* 1974). The validity of (A.1) is very good at the low densities considered here over a wide range of temperatures (approximately $70\,\mathrm{K} < T < 900\,\mathrm{K}$). The accuracy of the results is related to the signal-to-noise (S/N) ratio of the images and is about $\pm 5\%$ for the best images and $\pm 20\%$ for the worst cases, provided that the gas temperature is above 70 K; the accuracy can deteriorate by $(+20, -60\%)$ at very low gas temperatures Belan *et al* (2008, 2010). The constant k_g is obtained from direct calibrations (camera-dependent) on each tested gas. When working on monochromatic images, formula (A.1) must be used on image zones where the gas species is known, such as the ambient and the jet axis. Measurements in the mixing zones, where two gas species are usually present, are impossible for monochromatic images. They become possible if the light spectrum is analysed to determine the amounts of light given by each gas species, and

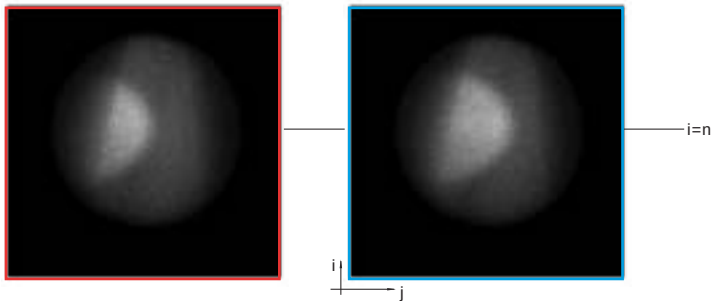

Figure B.1. A pair of successive images. The rows at $i = n$ are used for the correlation.

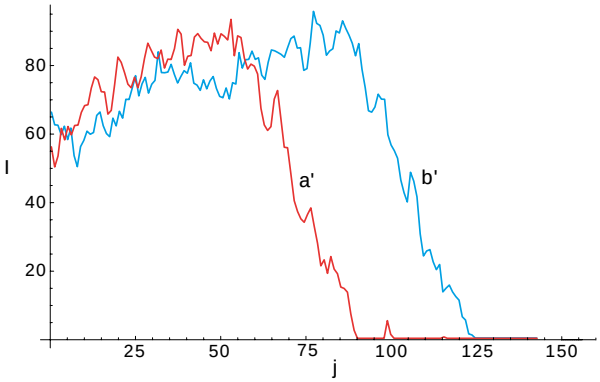

Figure B.2. Pixel intensities I versus pixel positions j for the two curves extracted from the original images at $i = n$.

this requires colour cameras (Belan *et al* 2008, 2010) or optical filters, at the price of a worse S/N ratio.

Appendix B. Image correlation techniques and velocity measurements

The velocity measurements have been obtained according to standard correlation procedures, as follows. A given pair of monochromatic images taken in succession (figure B.1) is represented by the relevant pixel matrices A_{ij} and B_{ij} of size $N \times N$. To determine the velocity of a moving structure, for example the jet head, each image must be cut at a suitable height, $i = n$, to intercept the structure under study, that is, along the line marked in figure B.1. This gives two rows, i.e. two pixel vectors or light intensity curves $a_j = A_{nj}$ and $b_j = B_{nj}$ (in general, pixel strips can be used instead of pixel rows to improve the S/N ratio). The moving part of these curves can be identified by subtracting the common offset c. These curves then become $a'_j = a_j - c$, $b'_j = b_j - c$ and are shown in figure B.2, with reference to a suitable shifted origin, since the absolute position of the origin does not affect the final correlation result, which is independent of translations.

However, a direct correlation still cannot be performed at this point because the second curve is not just a translation of the first one. To obtain a direct correlation, a cross-reflection

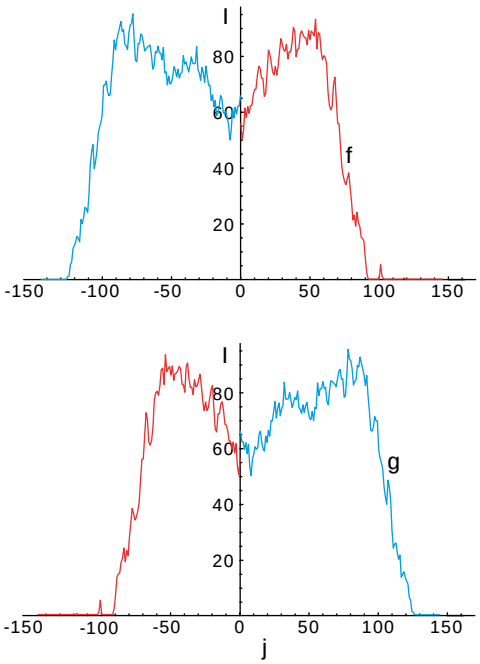

Figure B.3. Cross-reflection of the curves in figure B.2.

of the curves must be obtained with respect to the common origin and this gives rise to the new curves,

$$f_j = a'_j \cup R(b'_j), \quad g_j = b'_j \cup R(a'_j),$$

(see figure B.3), where R is a reflection or mirrored operator. The correlation can now be calculated as usual, i.e.

$$h_k = \sum_j f_j g_{k+j}, \quad k = 0, 1, \ldots, 2j_{\max}.$$

The resulting vector h_k (figure B.4) has a maximum at $k_{\max} = s$, where s (in pixels) is the structure shifts between the two images. The resulting velocity is $v = s/\Delta t$, where Δt is the interframe time.

The accuracy of this velocity measurement generally depends to a limited extent on the image noise and to a greater extent on the displacement d_e of the structure under test during the image exposure time t_e, that is, the uncertainty grows as $d_e = v\, t_e$. Here, the exposure cannot be lowered as desired because of the light level required; therefore, the uncertainties on the measured velocities may become remarkable, in particular for faster jets, such as underdense ones. All of the velocity measurements are presented together with their uncertainties, which are determined accounting for displacement effects and other minor error sources by uncertainty analysis, starting from the parameters of the film under test.

When the velocity of a structure is known, two successive images containing the same structure can also be superimposed after shifting the second one by s pixels, as in figure B.5. The same figure also shows that this procedure can be repeated, making use of different velocity measurements (head velocity, instability waves, etc). The jet structure can be spatially

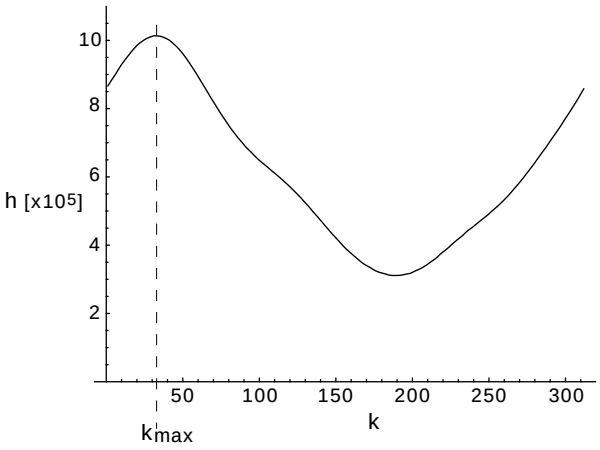

Figure B.4. The integral correlation curve h_k.

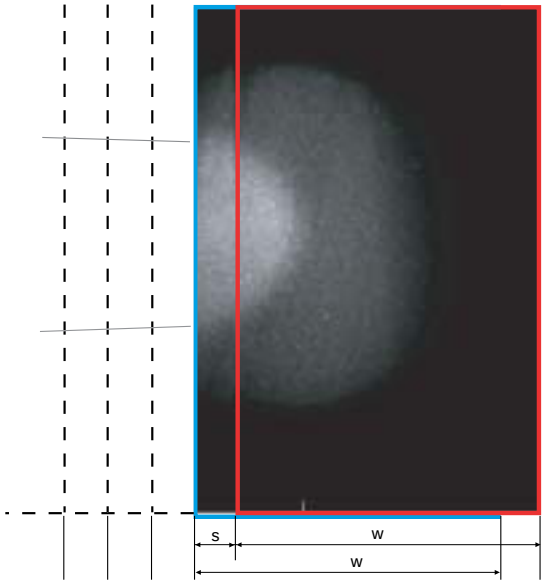

Figure B.5. Correlated superposition of the original images. Two vertical strips of equal width w are taken from the original images to discard pixels outside the electron blade in the left parts (w must be chosen once for an image series). The second (blue frame) strip is shifted to the left by s pixels and put below the first one (red frame). The procedure can be repeated, adding new strips from new images, which are always s pixels wide, and this leads to a jet image reconstruction.

reconstructed by superimposing parts of adjacent frames ('slices'). The reconstruction of the jet morphology at large scales has a physical meaning only if the changes in the structure properties are slow compared to the interframe time.

Appendix C. Film samples

A sample film is contained in movie 2 (available from stacks.iop.org/NJP/13/043011/mmedia), which shows an overdense xenon jet in argon, with $\eta = 73$, $\mathcal{M} = 13.5$. The exposure time is 195 μs, and the frame rate is 2100 s^{-1}. Movie 3 shows the same jet over a wider domain, and it has been obtained from the original one by means of multicorrelation techniques.

Appendix D. Details of the numerical method

We have modelled the transient injection conditions to mimic the actual behaviour of the mechanism described in figure A.2, expressing the stagnation pressure, through a fit of the experimental data, as a function of dimensionless time,

$$p_0(t) = a - b\,\mathrm{e}^{-c\,t/\tau} \tag{D.1}$$

($a = 1.21$, $b = 0.426$, $c = 0.00803$). This law accounts for the increase in p_0 during the piston run. At the end of this run, the valves open while the piston is still moving. The temporal modulation of the mass flow due to the opening of the valves can be expressed as

$$f(t) = 1 - \mathrm{e}^{-t/\tau T}, \tag{D.2}$$

where T is the time constant related to the mass flow initial growth, $T = 15$ for the light jet and $T = 3$ for the heavy one. The final decline in the flow rate in the jet was also modelled,

$$g(t) = \begin{cases} 1, & \text{if } t < \tau_S, \\ \dfrac{1}{\cosh(t/\tau - \tau_S/\tau)^{\beta}}, & \text{if } t \geqslant \tau_S, \end{cases}$$

where $\beta = 0.03$, $\tau_s = 55\tau$ for the light jet and $\tau_s = 70\tau$ for the heavy one. The dependence of the volumetric flow rate on time $Q(t)$ was obtained by modulating the ideal mass flow by the factor $p_0(t)\, f(t)\, g(t)$, as shown in figure 3 of the main paper.

In the increasing phase of the mass flow, the pressure, temperature and density of the gas at the nozzle exit p, T and ρ can be related in a simple way to the stagnation quantities p_0, T_0 and ρ_0 by means of the standard expansion law of gas dynamics. Furthermore, the stagnation quantities p_0, T_0 and ρ_0 are properties of the gas at the end of the piston compression, and they are related by the gas state law and by the isoentropic compression law, which holds because the motion of the piston is very fast. As explained above, $p_0(t)$ is a function of time and the dependence of p, T and ρ on p_0, T_0 and ρ_0 can be written, thanks to the mentioned equations, in the form

$$p \sim p_0(t), \tag{D.3}$$

$$T \sim T_0(t) \sim p_0(t)^{\gamma - 1}, \tag{D.4}$$

$$\rho \sim \rho_0(t) = p_0(t)/[R\,T_0(t)] \sim p_0(t)^{2-\gamma} \tag{D.5}$$

(R is the gas constant), which give for the mass flow

$$Q = \rho A v = \rho A \mathcal{M} c \sim p_0(t)^{1/2(3-\gamma)} = p_0(t)^{2/3}, \tag{D.6}$$

where γ can be set to 5/3 for the monoatomic gases considered here. For real valves, there is a pressure loss, expressed by the modulation factor (D.2), so that the real stagnation quantities are

$$p_{\mathrm{r}}(t) = p_0(t) f(t), \tag{D.7}$$

$$T_{\mathrm{r}}(t) = T_0(t) \sim p_0(t)^{\gamma-1}, \tag{D.8}$$

$$\rho_{\mathrm{r}}(t) = p_{\mathrm{r}}(t)/[R\, T_{\mathrm{r}}(t)] \sim p_0(t)^{2-\gamma} f(t) \tag{D.9}$$

and the mass flow at the nozzle output becomes

$$Q = \rho A v \sim p_0(t)^{1/2(3-\gamma)} f(t) = p_0(t)^{2/3} f(t). \tag{D.10}$$

When the mass flow is of the order of the reference mass flow yielded by the same nozzle under steady conditions, the modulation factor has the trend $f(t) \sim p_0(t)^{1/3}$, so that

$$p \sim p_r(t) \sim p_0(t)^{4/3}, \tag{D.11}$$

$$T \sim T_r(t) \sim p_0(t)^{\gamma-1}, \tag{D.12}$$

$$\rho \sim \rho_r(t) \sim p_0(t)^{(7-3\gamma)/3} \tag{D.13}$$

and finally

$$Q \sim p_0(t)^{(11-3\gamma)/6} = p_0(t), \tag{D.14}$$

$$v \sim p_0(t)^{1/2(\gamma-1)} = p_0(t)^{1/3} \sim Q^{1/3}. \tag{D.15}$$

D.1. Free boundary simulations and jet morphology

The authors have already studied the effects of the vessel walls by comparing different simulations of the same light jet obtained employing the actual lateral boundary conditions and the ones obtained from outflow conditions (see Belan *et al* 2011 and figure 10 therein). Very small differences in the density distribution morphologies are visible at the jet head, which appears slightly narrower in the free-boundary simulation, while the head positions differ by a few per cent in the two cases. Also, the effects of the shock reflection at the walls are weak, thanks to the large size of the vessel.

It is also worth noting that the head shape changes continuously with time, under both free-boundary and vessel-boundary conditions, because of the natural unsteadiness of the hypersonic flow behind the head (Massaglia *et al* 1996). As mentioned in the main paper, the jet head displacement is not continuous or smooth, even with a regular mass flow, but has impulsive behaviour, as can be seen in figure D.1. In the literature, this behaviour is often referred to as 'beam pumping'.

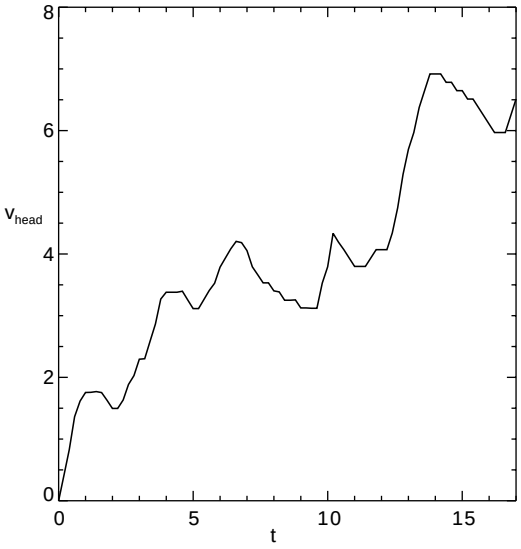

Figure D.1. Jet head velocity in dimensionless r_0/τ units versus dimensionless time for the light jet case and outflow lateral conditions.

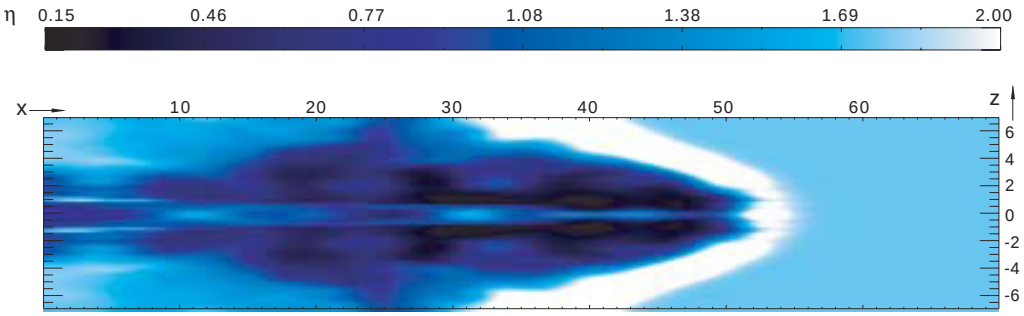

Figure D.2. Longitudinal 2D cut at $t = 15$ of the light jet simulation, processed by a longitudinal Gaussian convolution to simulate the integrated light acquired by the camera on the exposure time. The Gaussian half-width is 0.25 jet radii.

D.2. Comparison of the experiments and numerics: image convolution and cost

The numerical images presented in the main paper have been obtained directly from numerical calculations. In the comparison with the experimental data, it is possible to note the visualization apparatus effects, in particular of the finite and non-negligible exposure time of the camera. A simulation of the image downgrading can be obtained by convolving it with a Gaussian of half-width 0.25 jet radii, which accounts for the jet displacement that occurs during the opening time of the camera diaphragm. The result is shown in figure D.2, where the characteristic longitudinal blur of the jet head, due to camera exposure time, has been reproduced numerically.

We would like to end this appendix with a note on the cost in terms of time and money of the laboratory and numerical experiments that yielded the results presented in this paper. In the last ten years, we have observed a constant ratio between the two approaches. Both in time and in money, the laboratory costs are 5–6 time larger than that of the numerical simulations.

If we consider the whole costs, which includes for the laboratory the cost of the planning, the design, the building and acquisition of either the facility or the instrumentations, etc. . . , and the researchers costs, and for the simulations the HPC center CPU time and the researchers costs, we can estimate about 1×10^6 versus 2×10^5 euros. In both cases, the costs of the researchers sum to about the 50% of the total cost.

References

Belan M, De Ponte S, Massaglia S and Tordella D 2004 *Astrophys. Space Sci.* **293** 225–32

Belan M, De Ponte S and Tordella D 2008 Determination of density and concentration from fluorescent imges of a gas flow *Exp. Fluids* **45** 501–11

Belan M, De Ponte S and Tordella D 2010 Highly underexpanded jets in the presence of a density jump between an ambient gas and a jet *Phys. Rev.* E **82** 026303

Belan M, De Ponte S, Tordella D, Massaglia S, Ferrari A, Mignone A and Bodenschatz E 2011 Hydrodynamics of hypersonic jets: experiments and numerical simulations *Astrophys. Space Sci.* doi:10.1007/s10509-011-0600-6 http://www.springerlink.com/content/6307318x75507856/

Bellan P M, Livio M, Kato Y, Lebedev S V, Ray T P, Ferrari A, Hartigan P, Frank A, Foster J M and Nicolaï P 2009 *Phys. Plasmas* **16** 4

Birkinshaw M 1997 Instabilities in astrophysics jets *Advanced Topics on Astrophysical and Space Plasmas* ed E M Gouveia Dal Pino, A L Peratt, G A Medina Tancro and A C L Chian (Dordrecht: Kluwer) 17

Brown L O and Miller N 1957 α-Ray induced luminescence of gases *Trans. Faraday Soc.* **53** 748

Brown G L and Roshko A 1974 *J. Fluid Mech.* **64** 775

Bütefisch K A and Vennemann D 1974 The electron-beam technique in hypersonic rarefied gas dynamics, *Prog. Aerospace Sci.* **15** 217–55

Ciardi A, Lebedev S V, Frank A, Suzuki-Vidal F, Hall G N, Bland S N, Harvey-Thompson A, Blackman E G and Camenzind M 2009 *Astrophys. J.* **691** L147

Cocker R 2010 Laboratory astrophysics and scaling *Lecture Notes Phys.* **793** 1–28

Ferrari A 1998 *Annu. Rev. Astron. Astrophys.* **36** 539

Giannios D and Spruit H C 2006 *Astron. Astrophys.* **450** 887

Gouveia Dal Pino E M 2005 *Adv. Space Res.* **35** 908–24

Gregory C D, Howe J, Loupias B, Myers S, Notley M M, Sakawa Y, Oya A, Kodama R, Koenig M and Woolsey N C 2008 *Astrophys. J.* **676** 420

Grisnik S P 1998 Measurement of xenon viscosity as a function of low temperature and pressure *AIAA983498 34th Joint Propulsion Conf.* cosponsored by AIAA, ASME, SAE and ASEE *(Cleveland, OH, July 12–15, 1998)*

Hartigan P, Foster J M, Wilde B H, Coker B F, Rosen P A, Hansen J F, Blue B E, Williams R J R, Carver R and Frank A 2009 *Astrophys. J.* **705** 1073

Hollis B R 1966 Real-gas flow properties for NASA Langley Research Center aerothermodynamic facilities complex wind tunnels *NASA CR 4755* p 62

Kestin J, Knierim K, Mason E A, Najafi B, Ro S T and Waldman M 1984 Equilibrium and transport properties of the noble gases and their mixtures at low density *J. Phys. Chem. Ref. Data* **13** 229–54

Massaglia S, Bodo G and Ferrari A 1996 Dynamical and radiative properties of astrophysical supersonic jets. I: Cocoon morphologies *Astron. Astrophys.* **307** 997–1008

Matsakos T, Tsinganos K, Vlahakis N, Massaglia S, Mignone A and Trussoni E 2008 *Astron. Astrophys.* **477** 521–33

Matsakos T, Massaglia S, Trussoni E, Tsinganos K, Vlahakis N, Sauty C and Mignone A 2009 *Astron. Astrophys.* **502** 217–29

Mignone A, Bodo G, Massaglia S, Matsakos G, Tesileanu O, Zanni C and Ferrari A 2007 *Astrophys. J. Suppl.* **170** 228

Muntz E P 1968 The electron beam fluorescence technique *AGARDograph* TL500 N6 132, NATO, Paris. p 112

Reipurth B and Bally J 2001 *Annu. Rev. Astron. Astrophys.* **39** 403
Reipurth B, Heathcote S, Morse J, Hartigan P and Bally J 2002 *Astron. J.* **123** 362
Ricou F P and Spalding D B 1961 *J. Fluid Mech.* **11** 21–32
Sikora M, Begelman M C, Madejski G M and Lasota J P 2005 *Astrophys. J.* **625** 72
Sreenivasan K R and Prasad A K 2000 *Phys. Fluids* **12** 2101
Tordella D and Scarsoglio S 2009 *Phys. Lett.* A **373** 1159–64
Tzeferacos P, Ferrari A, Mignone A, Zanni C, Bodo G and Massaglia S 2009 *Mon. Not. R. Astron. Soc.* **400** 820–34
Turner J S 1986 *J. Fluid Mech.* **173** 431
Zanni C, Bodo G, Rossi P, Massaglia S, Durbala A and Ferrari A 2003 *Astron. Astrophys.* **402** 949
Zanni G, Ferrari A, Rosner R, Bodo G and Massaglia S 2007 *Astron. Astrophys.* **469** 811–28